

# Synchrotron Techniques in Interfacial Electrochemistry

BNL-49511

edited by

C. A. Melendres

Materials Science and Chemical Technology Divisions,  
Argonne National Laboratory,  
Argonne, Illinois, U.S.A.

and

A. Tadjeddine

CNRS, Laboratoire d'Electrochimie Interfaciale (Meudon)  
and  
LURE (Orsay), France



Kluwer Academic Publishers

Dordrecht / Boston / London

Published in cooperation with NATO Scientific Affairs Division

## SURFACE STRUCTURE AT THE Au(111) ELECTRODE

B. M. OCKO<sup>1</sup> and JIA WANG<sup>11</sup>

Brookhaven National Laboratory

Department of Physics<sup>1</sup>

Department of Applied Science<sup>11</sup>

Upton, New York 11973

### Abstract

This chapter summarizes Surface X-ray Scattering (SXS) studies carried out at the Au(111) surface under electrochemical conditions. In-plane diffraction measurements have been carried out to accurately determine the surface structures for bismuth and iodine adsorbate layers and for the reconstructed surface. Complementary x-ray specular reflectivity studies have been carried out to determine the surface normal structure. These studies are sensitive to the structure of the electrode and the solution layers.

### 1. Introduction

The electrode/electrolyte interface differs from the ultra high vacuum (UHV) interface in that the charge of the electrode surface can be controlled by adjusting the applied potential. At the electrochemical interface, electric fields as high as  $10^7$  V/cm are accessible, and the induced surface charge can exceed  $0.2$  e/atom. An understanding of the atomic scale structure of electrode surfaces is important in many fields of science and technology. However, until recently, structural investigations of electrode surfaces relied primarily on indirect methods (e.g., cyclic voltammetry (CV) and *ex situ* techniques such as low-energy-electron-diffraction (LEED)). During the past several years, surface x-ray scattering (SXS) [1-3], scanning tunneling microscopy (STM) [4-7], and atomic force microscopy (AFM) [8,9] techniques have been applied to single crystal electrode surfaces to study the electrodeposition of metals, the reconstruction of metal surfaces, the monolayer deposition of anion adlayers, the oxidation of metals, and the surface normal structure in the double layer region.

SXS is an extension of bulk x-ray scattering [10] which incorporates the semi-infinite nature of real crystals. The broken translational symmetry of the interface gives rise to weak scattering which can be distinguished from the more intense three dimensional bulk Bragg peaks. For the reader unfamiliar with surface x-ray scattering, there are several excellent reviews [11]. In addition to these more general reviews, several reviews pertaining to the electrochemical environment are recommended [12].

The structure of surfaces can be investigated with SXS within the surface plane and along the surface normal by controlling the direction of the scattering vector  $\vec{Q}$ , which is the difference between the incident and scattered x-ray wave vectors. Typically, information within the surface plane is obtained by orienting  $\vec{Q}$  almost entirely within the surface plane.

This corresponds to the grazing incidence angle geometry where the grazing incidence angle is typically a few degrees. On the other hand, when  $\vec{Q}$  is aligned entirely along the surface normal direction (e.g., no in-plane component) information is obtained about the surface normal structure. This geometry is referred to as specular reflectivity since the angle between the surface plane and incident wave vector is equal to the angle between the surface plane and the scattered wave vector. Additional structural information can be obtained by determining the scattered intensity distribution along the surface normal direction at a fixed, finite in-plane wave vectors corresponding to either the bulk crystal structure or to the overlayer structure.

This chapter is intended to review SXS electrochemical studies carried out at the Au(111) surface. In section 2, a brief review of the electrochemical and x-ray scattering techniques is provided. In the following section the structures within the surface plane, obtained from grazing incident angle diffraction measurements, are presented and in the last section the surface normal electrode and solution phase structures, obtained from x-ray reflectivity measurements, are presented. At the Au(111) surface both hexagonal and rectangular structures have been reported in the literature, however, this chapter is limited to uniaxial-incommensurate-rectangular (UIR) ( $p \times \sqrt{3}$ ) structures. Here we present results for the reconstructed Au surface and for Bi, and I adlayers on the ideally terminated surface. Due to the high resolution of SXS, we are able to show that the iodine and bismuth adlayers are continuously compressible over a range of potential and that they show no "lock-in" transitions at commensurate lattice positions.

The x-ray specular reflectivity technique is presented in section 3.2 and results are shown for a variety of solutions. Here we explain the relationship between the surface normal structure and specular reflectivity with particular attention to simple density profiles. Analysis of the reflectivity profiles suggests that the first layer of water exhibits enhanced positional order. For an iodine adlayer, the iodine coverage, deduced from the reflectivity analysis, agrees with the value obtained from the in-plane diffraction study.

## 2. Experimental Techniques

### 2.1. SURFACE PREPARATION AND ELECTROCHEMICAL CONDITIONS

A gold disk electrode (10 mm diameter by 2 mm) was spark cut and aligned along the normal [111] direction [13]. The disk was aligned within  $0.1^\circ$  of the (111) axis, mechanically polished, and then electropolished [15]. Finally, the crystal was sputtered using an argon beam at  $5 \times 10^{-5}$  torr at  $800^\circ\text{C}$  using a defocused beam at 1 keV and  $2 \times 10^{-6}$  A for several hours. The sample was transferred through air to an electrochemical x-ray scattering cell constructed from Kel-F as shown in Fig. 1.

A 6  $\mu\text{m}$  polypropylene window sealed the cell with a thin capillary electrolyte film between the crystal face and the polypropylene film. An outer chamber was flushed with  $N_2$  gas to prevent oxygen from diffusing through the polypropylene membrane. The applied potential was referenced to a Ag/AgCl (3M KCl) electrode connected to the cell through a micro glass frit. In order to reduce the possibility of chloride contamination from the reference electrode, a second frit was added and the path separating the two frits was filled with NaF electrolyte. Counter electrodes were either gold or platinum wires.

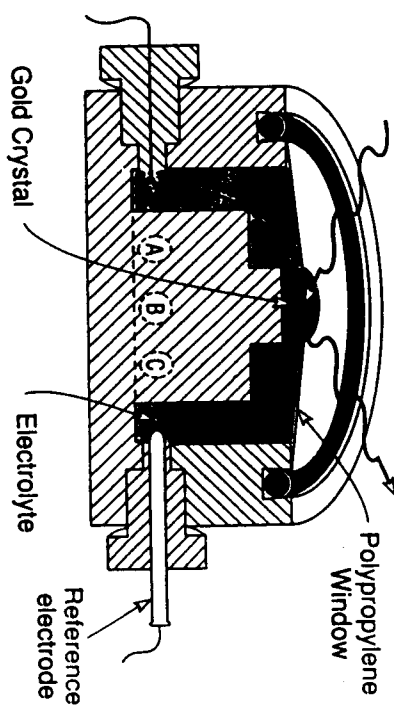


Figure 1. X-ray electrochemical cell.

After flushing the cell with  $N_2$  gas, the deoxygenated electrolyte was injected into the cell using a syringe. The cell was filled with enough solution to expand the polypropylene window leaving a thick electrolyte layer (several mm) between the face and the window. The potential control was then turned on and cyclic voltammograms were carried out in this geometry to check the electrochemical conditions. Before carrying out the x-ray scattering measurements the cell was deflated leaving a thin electrolyte layer which we estimate from the small angle reflectivity measurements to be between 10 and 20  $\mu$  thick. In this thin electrolyte layer geometry, the effects of bulk impurities are greatly reduced relative to the thick electrolyte geometry.

### 2.2. X-RAY SCATTERING

The x-ray scattering measurements were carried out with focused, monochromatic synchrotron radiation at beam lines X22B, X22C, and X25 at the National Synchrotron Light Source (NSLS) at Brookhaven National Laboratory. In the four circle geometry, the sample was oriented through its Euler angles  $\theta$ ,  $\chi$ , and  $\phi$  by a spectrometer under computer control [11,16,17]. The magnitude of the scattering wave vector is  $|\vec{k}_f - \vec{k}_i| = (4\pi/\lambda)\sin(2\theta/2)$ , where  $\vec{k}_i$  and  $\vec{k}_f$  correspond respectively to the incident and scattered wave vectors and where  $2\theta$  is the angle between these two vectors [10]. Diffraction measurements were carried out by measuring the scattering intensity along paths in reciprocal space in the " $w = 0$  geometry" [18].

To conveniently describe the scattering wave vector in terms of its components in and out of the surface plane, we employ a hexagonal coordinate system [13,19]. In this coordinate system, an arbitrary position in hexagonal reciprocal space (see Fig. 2) is represented by the vector ( $H, K, 0$ ) within the surface plane and  $(0, 0, L)$  along the surface normal

direction. The reciprocal space lattice constants are  $a^* = b^* = \frac{4\pi}{a\sqrt{3}} = 2.52 \text{ \AA}^{-1}$ , and  $c^* = \frac{2\pi}{a\sqrt{3}} \approx 0.89 \text{ \AA}^{-1}$  where  $a = 2.885 \text{ \AA}$  is the gold nearest-neighbor spacing. The relationship between the cubic vector,  $(h, k, l)_{\text{cubic}}$ , and the hexagonal vector  $(H, K, L)$  is given by the transformations  $h = -4H/3 - 2K/3 + L/3$ ,  $k = 2H/3 - 2K/3 + L/3$ , and  $l = 2H/3 + 4K/3 + L/3$ . For example,  $(1, 1, 1)_{\text{cubic}} = (0, 0, 3)$ ,  $(0, 0, 2)_{\text{cubic}} = (0, 1, 2)$ , and  $(0, 2, 2)_{\text{cubic}} = (1, 0, 4)$ .

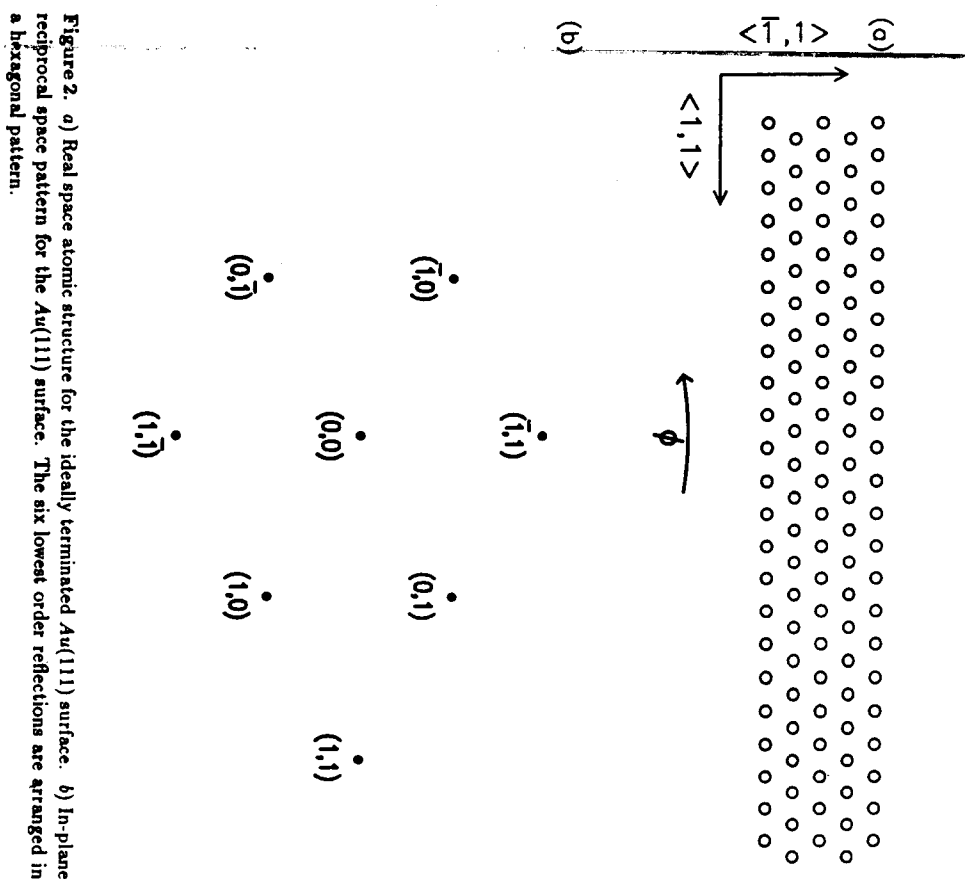


Figure 2. a) Real space atomic structure for the ideally terminated Au(111) surface. b) In-plane reciprocal space pattern for the Au(111) surface. The six lowest order reflections are arranged in a hexagonal pattern.

### 3. Results

#### 3.1. IN-PLANE DIFFRACTION STUDIES

Despite the underlying hexagonal symmetry of the Au(111) surface, the top layer of atoms often forms a uniaxial incommensurate rectangular (UR) phase. This phase, is denoted  $(p \times \sqrt{3})$  since the repeat distances, in units of the nearest-neighbor distance ( $a$ ), are  $p$  and  $\sqrt{3}$ . In the following three subsections, we present detailed information on the in-plane structure and phase behavior of the  $(p \times \sqrt{3})$  UR phases for the reconstructed surface (no specifically adsorbed species), for adsorbed bismuth adlayers, and for adsorbed iodine adlayers.

There are three equivalent rectangular surface domains which may form on the underlying hexagonal substrate and all three contribute to the observed diffraction patterns. For simplicity, only the domain for which the incommensurate direction is along the (110) direction will be considered. The in-plane measurements were carried out in the grazing incident angle geometry with a grazing incident angle,  $\alpha$ , equal to  $1.25^\circ$ . This angle corresponds to  $L = 0.2$  at all wavelengths. In this section, three dimensional wavevector  $(H, K, 0.2)$  will be referred to as  $(H, K)$ .

At a grazing angle of  $1.25^\circ$  the incident x-rays illuminate a region of the crystal  $0.5 \text{ mm}$  wide across the entire crystal face ( $10 \text{ mm}$ ). The spectrometer resolution, in reciprocal space, was primarily determined by the angular acceptance of the scattered radiation and the mosaic of the Au(111) crystal. Within the scattering plane the spectrometer resolution was determined by an array of equally spaced parallel plates (Soller slits) which provide a  $2\theta$  resolution of  $0.1^\circ$  half-width-half-maximum (HWHM). The scattered intensity was measured with a scintillator detector on the  $2\theta$  arm following the Soller slits.

#### 3.1.1. Au(111) SURFACE RECONSTRUCTION

The possibility that gold surfaces might reconstruct under electrochemical conditions was suggested on the basis of the hysteresis in capacity-potential curves [20]. *Ex situ* LEED studies have shown that the Au(111) surface, after emersion from an electrochemical cell, forms a  $(23 \times \sqrt{3})$  phase in the negative potential regime [21]. *In situ* STM studies [5] in  $\text{HClO}_4$  solutions have confirmed the existence of the  $(p \times \sqrt{3})$  reconstruction within the negative potential regime. The real space structure of the reconstructed Au(111) surface is shown in Fig. 3a.

In a surface diffraction measurement, the  $(p \times \sqrt{3})$  reconstruction gives rise to additional in-plane reflections beyond the underlying  $(1 \times 1)$  reflections. These are arranged in a hexagonal pattern (see Fig. 3b) around the integer reflections [13,14]. Here we limit our discussion to diffraction along the  $q_x$  axis, see Fig. 3b, which connects the reconstruction peak at  $(\delta/\sqrt{3}, 1 + \delta/\sqrt{3})$  to the  $(0,1)$  peak. In Fig. 4a, the measured scattering intensity is shown at a series of decreasing potentials between  $0.1$  and  $-0.8 \text{ V}$  in a  $0.01 \text{ M NaCl}$  solution. At potentials of  $0.10 \text{ V}$  and above, the scattering is centered at  $q_x = 0$ , which indicates that the surface is not reconstructed. As the potential is reduced below  $0.05 \text{ V}$ , a second peak emerges, which signals the reconstructed phase. The reconstruction peak position,  $(\delta/\sqrt{3}, 1 + \delta/\sqrt{3})$ , moves outward corresponding to increased compression as the potential is decreased.

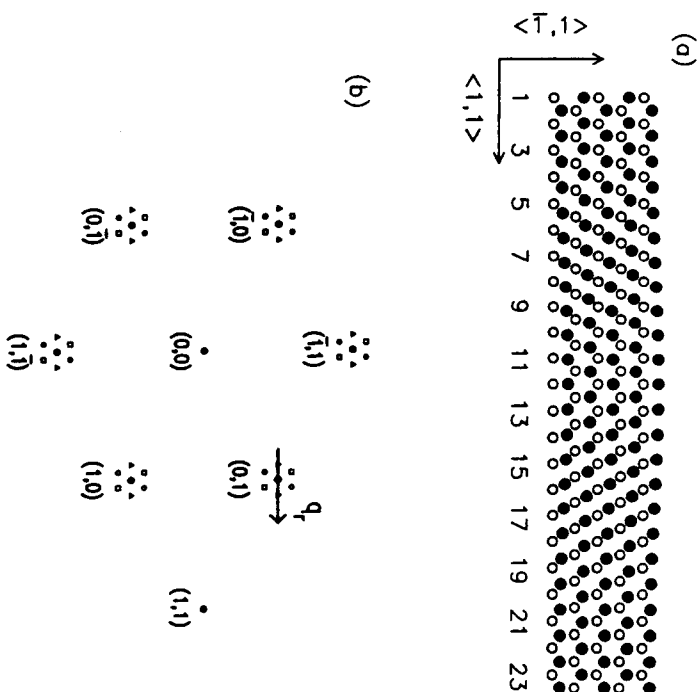


Figure 3. a) Real space structure of the reconstructed  $(p \times \sqrt{3})$  Au(111) surface are shown as filled circles. Surface atoms in the left and right hand sides of the figure are in undistorted hexagonal sites (ABC stacking sequence). In the center of the figure the surface atoms are in faulted sites (ABA stacking sequence) [19]. For 24 surface atoms in place of 23 underlying surface atoms along the (11) direction, the compression is  $24/23 - 1 = 4.4\%$  and  $\delta = (\sqrt{3}/2)/23 = 0.038$ . b) Reciprocal space pattern for reconstructed Au(111) surface. In addition to the hexagonal pattern from the underlying Au(111) layers (filled circles), the reconstructed surface exhibits reflection arranged in a hexagonal pattern (open symbols) surrounding the filled circles. Diffraction data was acquired by carrying out scans along the  $q_z$  direction in reciprocal space.

In order to extract the unit cell size  $p$  (referred to as the stripe separation) the scattering profiles have been described as the sum of two Lorentzians [13,14] (centered at zero and  $\delta$ ). Fits to the Lorentzian form (solid lines in Fig. 4a) describe most of the essential features of the profiles. The dependence of the fitted stripe separation,  $p = \sqrt{3}/(2\delta)$ , is

shown in Fig. 4b. Although the transition is reversible, the measured stripe separation depends on the sweep direction, as indicated in the figure. After the initial signs of the surface reconstruction at 0.05 V (corresponding to the emergence of the reflection at  $(\delta/\sqrt{3}, 1 + \delta/\sqrt{3})$ ), there is further compression as the potential is decreased, as shown by the inverted triangles in Fig. 4b. The maximum observed compression corresponds to  $p = 23$  ( $\delta = 0.038$ ). This length is identical to that found in vacuum studies. This observation suggests that the Au(111) surface has the same underlying surface motif under electrochemical and vacuum conditions.

The reconstruction formation/lifting transition can be directly related to the induced surface charge,  $\sigma(E)$ , independent of the anion species. The induced surface charge density has been obtained by integrating the capacitance curve from the PZC to  $E$ , that is,  $\sigma(E) = \int_{PZC}^E C(E') dE'$ . This relation is correct in weakly adsorbing electrolytes and nonadsorbing electrolytes, such as in a 0.1 M NaF electrolyte. At a surface charge density of  $\approx 0.07$  e/atom (excess electrons), in all solutions, the reconstruction starts to lift at  $\sigma = +0.07$  e/atom. This lifting transition occurs at  $\sigma = +0.05$  e/atom in NaBr solutions. The appearance of the reconstructed surface at a common value of  $\sigma$ , in all the three electrolytes, suggests a simple phase transition mechanism based on the excess surface charge.

The idea that excess surface charge might induce surface atoms to form a structure different than the underlying bulk layers has been discussed in calculations by Fu and Ho using a local-density-functional (LDF) model [22]. For Ag(110) they predicted that the missing-row structure – absent at the clean metal surface – is induced by alkali adsorbates with an induced surface charge of  $\approx 0.05$  e/atom. Within the context of the LDF model, adsorbates in vacuum mimic an applied electric field.

### 3.1.2. BISMUTH ADLAYERS ON THE Au(111) ELECTRODE

During the electrodeposition process metal ions may be adsorbed and reduced at potentials positive of the bulk deposition potential. The metal adlayers which form under these conditions, referred to as underpotential deposition (UPD), are most often monolayer phases, however, in several instances bilayer phases may also form. The UPD potential range can extend over a one volt potential window and over this range there may be several different structures. These structures may exhibit either long range or short range positional order and in some instances island deposits may form.

The first in situ in-plane diffraction studies of a UPD structure were carried out by the IBM Almaden group on epitaxial Ag(111) films [1]. These studies showed for the first time that UPD lead layers exhibit an incommensurate, hexagonally close packed structure (hcp) and that the lead-lead spacing could be modified by the applied potential. Chen and Gewirth had previously utilized AFM to show that two distinct UPD Bi adlattice structures exist on the Au(111) electrode surface [9]. As the potential is decreased, a commensurate  $(2 \times 2)$  adlattice first appears which exhibits a 25% coverage. At more negative potentials (but positive of the bulk electrodeposited bismuth phase) a second bismuth adlattice appears which is rectangular (see Fig. 5a).



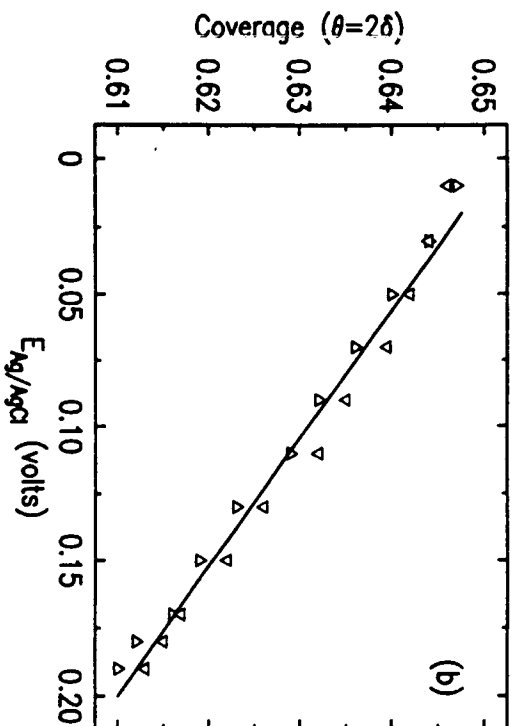
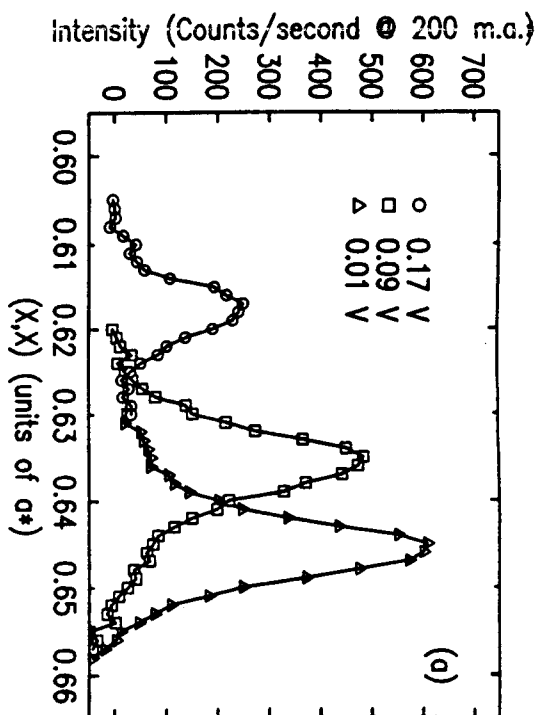


Figure 6. (a) X-ray scattering profiles for the bismuth ( $p \times \sqrt{3}$ ) adlayer on the Au(111) surface along the (11) direction at three potentials after background subtraction. (b) The bismuth coverage,  $\theta = 2\delta = p^{-1}$ , obtained by measuring the peak position ( $2\delta, 2\delta$ ) versus the applied potential. The triangles and inverted triangles correspond to the positive and negative potential sweeps, respectively.

The atomic coverage of Bi can be measured very accurately from the diffraction peaks shown in Fig. 6a since the coverage  $\theta$ , relative to the underlying gold density, is equal to  $2\delta$  [23]. Diffraction data was acquired along the (11) direction every 20 mV. On the Ag/AgCl potential scale bulk deposition occurs very close to zero volt. In Fig. 6b, the bismuth coverage is shown in the positive potential sweep (triangles) and in the negative potential sweep (inverted triangles). When the ( $p \times \sqrt{3}$ ) phase first appears at 0.19 V,  $\theta = 0.612$ . As the potential is lowered the coverage continuously increases in a linear manner with decreasing potential. The line shown in Fig. 6b is a linear fit to the data with an electrocompressibility  $d\theta/dE = -0.208/V$ . This slope is about 30% larger at the Au(111) surface than for the Ag(111) surface [2]. At 0.01 V, just prior to bulk deposition,  $\theta = 0.646$  which corresponds to a Bi lattice constant of  $a/(2\delta) = 4.48 \text{ \AA}$ . The lattice constants of gold and silver only differ by 1/4% and not surprisingly the Bi adlayer achieves the same lattice constant on both the Ag and Au (111) surfaces before bulk deposition appears [2].

### 3.1.3. IODINE ADLAYERS ON THE Au(111) ELECTRODE

Recently, in situ STM studies have been extended to adsorbed iodine adlayers at the Au(111) surface. A centered-rectangular ( $5 \times \sqrt{3}$ ) and a rotated-hexagonal ( $7 \times 7$ )  $R 21.8^\circ$  structure has been reported by Gao and Weaver [7] whereas a ( $\sqrt{3} \times \sqrt{3}$ )  $R 30^\circ$  and ( $3 \times 3$ ) has been published by Tao and Lindsey [6]. Here, we show that adsorbed iodine on the Au(111) surface forms an electrocompressive UIR ( $p \times \sqrt{3}$ ) phase. The key results of our SXPS studies of electrodeposited iodine on the Au(111) surface are presented below. The complete study will be published elsewhere [25].

The present study was carried out in 0.01 M potassium iodide ( $KI$ ) solutions. Within the ( $p \times \sqrt{3}$ ) rectangular phase the diffraction pattern [25] is given by the basis vectors  $\delta$ ,  $\delta$  and  $(\frac{1}{2}, \frac{1}{2})$ , where the iodine coverage  $\theta = 2\delta = 1/p$ . Since half of the spots are absent in the pattern shown in Fig. 7b (i.e., complete cancellation of the scattering amplitudes) the real space unit cell is centered with two iodine atoms (see Fig. 7a). Along the (11) direction the first diffraction reflection is at  $(2\delta, 2\delta)$  where  $2\delta \approx 0.39$ . We note that the ( $5 \times \sqrt{3}$ ) structure (four atoms per unit cell) is identical to the ( $p \times \sqrt{3}$ ) structure (two atoms per unit cell) when  $p = 2.5$  ( $2\delta = 2/5$ ), and the commensurate ( $\sqrt{3} \times \sqrt{3}$ )  $R 30^\circ$  structure is identical to the ( $p \times \sqrt{3}$ ) structure when  $p = 3$  ( $2\delta = 1/3$ ). At all potentials the ( $\sqrt{3} \times \sqrt{3}$ )  $R 30^\circ$  structure, expected on the basis of previous studies [21], was never observed.

Typical x-ray scattering profiles of the incommensurate-rectangular iodine phase through the peak at  $(2\delta, 2\delta)$  are shown in Fig. 8a. The sharp diffraction peak in the profiles originates from rows of iodine atoms which are separated by  $pa/2$  as shown in Fig. 7a. As the potential is increased these diffraction peaks shift to larger  $\delta$  in a uniform manner. The coverage,  $\theta$ , relative to the underlying Au(111) layers is equal to  $2\delta$ . In Fig. 8b the coverage is shown for both the positive and negative sweep directions. There is a slight shift in  $\theta$  obtained from positive and negative sweep directions by about 0.1%. This suggests that there is a fundamental difference between adding atoms (positive sweep) relative to removing atoms (negative sweep).

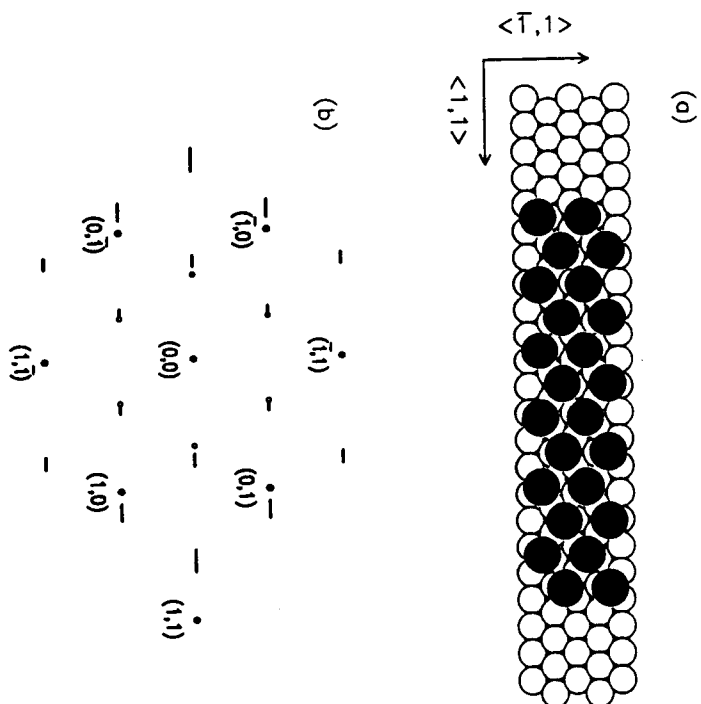


Figure 7. a) Real space atomic structure for the  $(p \times \sqrt{3})$  iodine adlayer on the  $\text{Au}(111)$  surface. b) In-plane reciprocal space pattern for the  $\text{Au}(111)$  surface with a centered  $(p \times \sqrt{3})$  iodine adlayer. The underlying gold layers yield the integer reflections (filled circles) whereas the iodine adlayer yields the reflections shown by the short line segments.

At a critical coverage of 0.409 the  $(p \times \sqrt{3})$  phase transforms to a rotated-hexagonal phase in which the adsorbed iodine atoms no longer remain in the hollow gold rows [25]. This transition can be understood in terms of the competition between the  $I-I$  and the  $I-Au$  interactions. Within the  $(p \times \sqrt{3})$  phase the nearest iodine atoms (four) are in neighboring rows where the  $I-I$  distance,  $D_{I-I} = a\sqrt{\frac{1}{3} + \frac{\sqrt{3}}{2}}$ , varies from 4.62 to 4.32 Å as  $\theta$  varies from 0.366 to 0.409. The next nearest iodine atoms (two) are always displaced by two gold rows, i.e.,  $a\sqrt{3} = 4.998$  Å. The transition to the rotated-hexagonal phase appears at a potential when  $D_{I-I} = 4.32$  Å is very close to the Van der Waals diameter of 4.30 Å. At this bond length the energy required to pack the adatoms closer can no longer offset

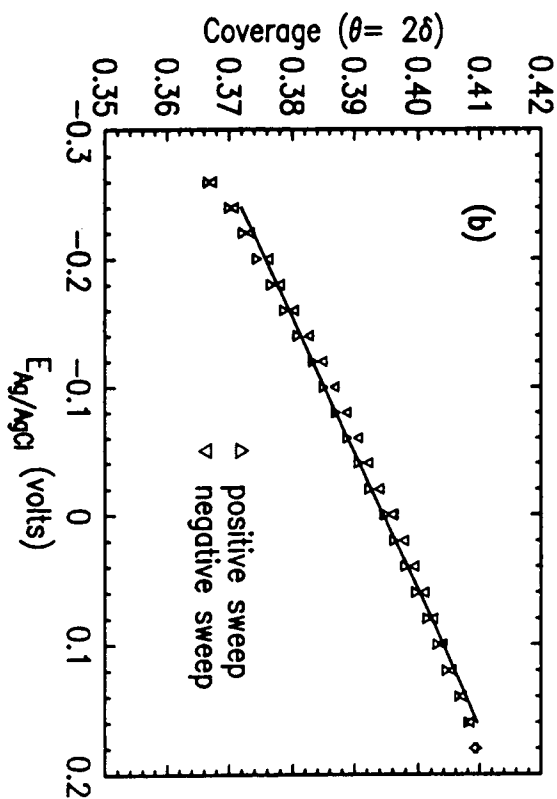
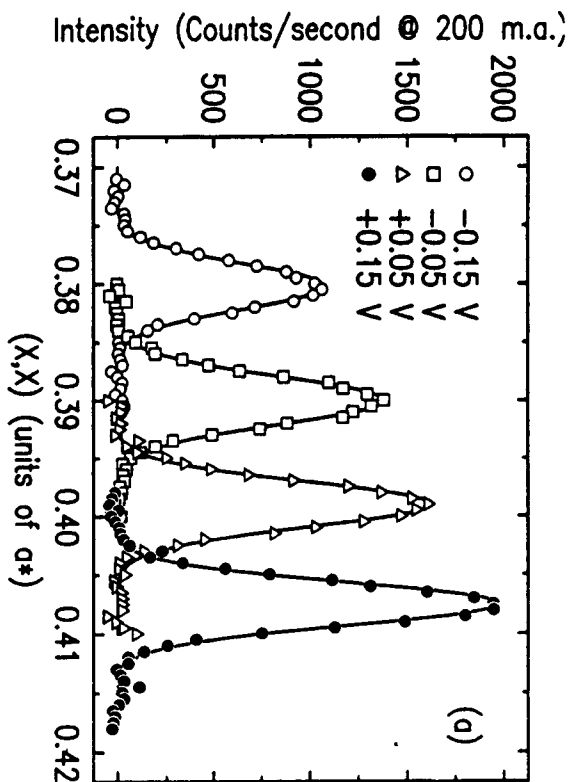


Figure 8. (a) X-ray scattering profiles for the iodine  $(p \times \sqrt{3})$  adlayer on the  $\text{Au}(111)$  surface along the  $(11)$  direction at four potentials after background subtraction. (b) The iodine coverage,  $\theta = 2\delta = p^{-1}$ , obtained by measuring the peak position  $(2\delta, 2\delta)$  versus the applied potential. The triangles and inverted triangles correspond to the positive and negative potential sweeps, respectively.

the adsorbate-substrate energy gained by maintaining the  $I$  atoms in the hollow gold rows and the transformation to the rotated-hexagonal phase proceeds.

From the STM studies it is difficult to ascertain whether the incommensurate structures "lock in" to the commensurate structures [6, 7]. In the present SXS measurement a "lock in" transition would be manifested by a region of potential in which there is no change in the unit cell. However, as demonstrated by Fig. 8b there is no indication of a change in the monotonic increase in  $2\theta$  with potential at the commensurate ( $5 \times \sqrt{3}$ ) structure ( $2\theta = 0.4\theta$ ). A linear fit to the coverage versus potential plot is shown in Fig. 8b as the solid line. The electrocompressibility  $d\theta/dE = 0.094/\text{V}$  which is about a factor of two smaller in magnitude than for Bi on the Au(111) surface.

For the bismuth and iodine adlayers we have also compared the areal slope ( $dA/dE$ ). The area per adsorbed atom  $A = a^2\sqrt{3}\theta^{-1}$  and  $dA/dE = 7.21 \text{ \AA}^2(-d\theta/dE)/ < \theta >^2$ . For the bismuth and iodine adlayers  $|dA/dE|$  equals  $3.75 \text{ \AA}^2/\text{eV}$  and  $4.47 \text{ \AA}^2/\text{eV}$ , respectively. This finding shows that there is better agreement for  $|dA/dE|$  than for  $d\theta/dE$  when comparing bismuth and iodine adlayers. At the present time, no model or theory adequately describes the observed electrocompressibility of electrodeposited adlayer phases.

### 3.2. X-RAY REFLECTIVITY

Specular x-ray reflectivity has been successfully applied to many different types of interfaces including the solid/vacuum [19,26], solid/vapor, liquid/vapor [27], and solid/liquid interfaces [3,13,14,28]. Reflectivity is a powerful probe of interfacial structure since it can be related to the average electron density profile along the surface normal axis in a straight forward manner. As previously demonstrated, at an electrochemical interface the reflectivity depends on the structure of the underlying atomic layers and of surface adsorbates [13]. Quantitative information on the layer spacings, densities, and root-mean-square (r.m.s.) displacement amplitudes can be obtained by fitting the reflectivity profiles to simple real space models. In Fig. 9 the atomic structure of the ideally terminated Au(111) surface is shown and the corresponding reciprocal space pattern. Before describing the measured reflectivity spectra from the Au(111) surface (section 3.2.3), the relationship between the surface normal electron density and reflectivity is shown (section 3.2.1). The experimental aspects of obtaining reliable reflectivity spectrums are presented in section 3.2.2.

#### 3.2.1. SIMPLE REFLECTIVITY MODELS

First we consider the theoretical specular reflectivity for an ideally terminated Au(111) surface. Within the kinematical approximation (also known as the Born approximation), the absolute specular reflectivity can be calculated from a sum over atomic layers. As previously shown [19,13], for the ideally terminated Au(111) surface the reflectivity is given by

$$R(L = Q_z/c^*) = |T(Q_z)|^4 \left| \frac{256\pi^2 r_e^2}{3a^2 Q_z^2} \right| \left| F_{Au}(Q_z) e^{-\frac{1}{2} Q_z^2 \sigma_{DB}^2} s(Q_z) \right|^2 \quad (1)$$

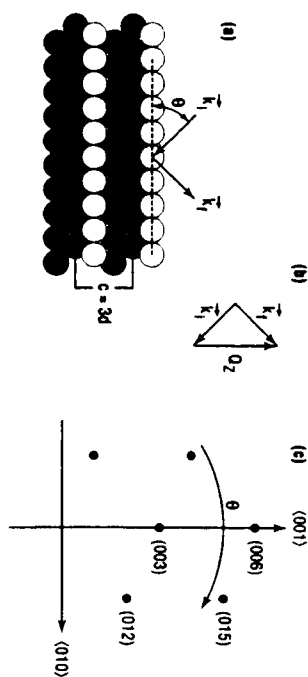


Figure 9. a) Surface normal atomic structure for the ideally terminated Au(111) surface.  $\vec{k}_i$  and  $\vec{k}_f$  are the incident and outgoing wavevectors, respectively, and in b)  $\vec{Q}_z$  is the momentum transferred. c) The corresponding reciprocal space pattern. The arc corresponds to a  $\theta$  rocking curve path in reciprocal space.

where  $r_e$  is the Thomson radius of the electron,  $F_{Au}(Q_z)$  is the atomic form factor of gold, and  $\sigma_{DB} = 0.085 \text{ \AA}$  is the r.m.s. displacement amplitude (Debye-Waller term) [29]. The sum over atomic layers is given by

$$s(Q_z) = \sum_{n=0}^{\infty} e^{iQ_z n d} \quad (2)$$

where  $d = 4.08 \text{ \AA}/\sqrt{3}$  for gold. Carrying out the geometric sum over the atomic layers gives the relationship

$$|s(L)| = \frac{1}{2} \left| \sin\left(\frac{\pi L}{3}\right) \right|^{-1} \quad (3)$$

where  $L = Q_z/c^*$ . We point out that  $|s(L)|$  is a measure of the number of gold layers which add coherently. When  $L$  is midway between two Bragg peaks the geometric sum  $|s(L)|$  is  $\frac{1}{2}$  and the scattered intensity corresponds to the equivalent scattering from half a monolayer of gold. Bragg peaks emerge from Eqs. 1-3 when  $L = 3n$  (where  $n$  is an integer) since the sum diverges when the scattering from all the atomic layers are in phase. The kinematical approximation is unphysical in the vicinity of Bragg peaks since the reflectivity can be greater than unity. In order to correct the model, the dynamical model of x-ray scattering, which takes into account the decrease in the incident electric field as a function of the penetration depth, must be utilized [10]. However, the kinematic approximation provides a good approximation to the dynamical model when the reflectivity is less than 0.1% of the incident beam. An important feature of both models is the  $(L - 3n)^{-2}$  dependence of the reflectivity in the tails of the Bragg peaks.



In Fig. 10a we show the calculated  $R(L)$  for the ideally terminated  $Au(111)$  surface and the corresponding real space layer profile. The principal features are the Bragg peaks (divergence), the weak scattering between neighboring Bragg peaks, and the nearly 100% reflectivity at small  $L$ . For reconstructed or otherwise non-ideally terminated surfaces, the scattering amplitudes from the atomic layers close to the surface are no longer equivalent to the bulk scattering amplitudes. We now consider the possibility that the top gold layer is different from all of the ideally terminated underlying gold layers [26].

In the single-layer model, we express the sum over atomic layers as

$$s(Q_z) = \rho_1 e^{iQ_z d_1} (\sigma_{BS}^2 - \sigma_1^2) e^{iQ_z d_1} + \sum_{n=1}^{\infty} e^{iQ_z n d} \quad (4)$$

where the top layer density ( $\rho_1$ ), the top layer  $Au-Au$  interlayer spacing ( $d - d_1$ ), and the top layer layer r.m.s. displacement amplitude  $\sigma_1$  may differ from their ideal values of 1, 2.355 Å, and 0.085 Å, respectively. Here we consider separately the effects of each parameter. Finally, we note that for real surfaces all three effects are important.

First, we consider how changes of the interlayer expansion or contraction of the top gold layer modify the reflectivity profiles. We consider the examples in which  $\rho_1$ , and  $\sigma_1$  are equal to their bulk values and  $d = 0.1 d$  (a 10% expansion). In Fig. 10b we show the density and reflectivity profiles for this model as solid lines and the ideal profiles are shown as dotted lines. The most striking feature of the reflectivity profile for the expanded top layer model, shown by the solid line, is the asymmetry in the vicinity of the Bragg peaks. Here the reflectivity is enhanced to the left of the Bragg peak and reduced on the right side. Note that the asymmetry increases as the order of the Bragg peak increases. Furthermore, the asymmetry increases as the top layer expands and the asymmetry reverses if the top layer contracts.

Secondly, we consider how the r.m.s. displacement amplitude of the top gold layer modifies the reflectivity profiles. Here, as an example, we present the case where  $\sigma_1$  is increased from its bulk value of 0.085 Å [29] to 0.40 Å and where  $\rho_1$ , and  $d_1$  are equal to their bulk values. This effectively redistributes the gold atoms such that there is a greater range of scattered phase factors from the top gold layer relative to the underlying gold layers. In Fig. 10c we show the density and reflectivity profiles for this model as solid lines and the ideal profiles are shown as dotted lines. The enhanced r.m.s. displacement model reflectivity curve is always less than the ideally terminated curve and this reduction is most significant at intermediate wavevectors between Bragg peaks and increases with  $L$ . Within the context of Eq. 4, an enhanced r.m.s. displacement amplitude decreases the magnitude of the scattering amplitude of the top layer relative to the underlying layers and this effect increases with  $L$ . For sufficiently large  $L$  the Gaussian factor,  $e^{-Q_z^2 \sigma_0^2/2}$ , approaches zero and the scattering amplitude from the top layer no longer contributes to the sum. At this point, the reflectivity approaches the ideally terminated reflectivity profiles (not shown in the figure).

Finally, we consider how the density of the top gold layer modifies the reflectivity profiles. Here, as an example, we present the case where the top layer density,  $\rho_1$  is decreased from its bulk value of unity to  $\frac{1}{2}$  and where  $\sigma_1$ , and  $d_1$  are equal to their bulk value. Physically, this half-density occurs when there is a missing-row reconstructed

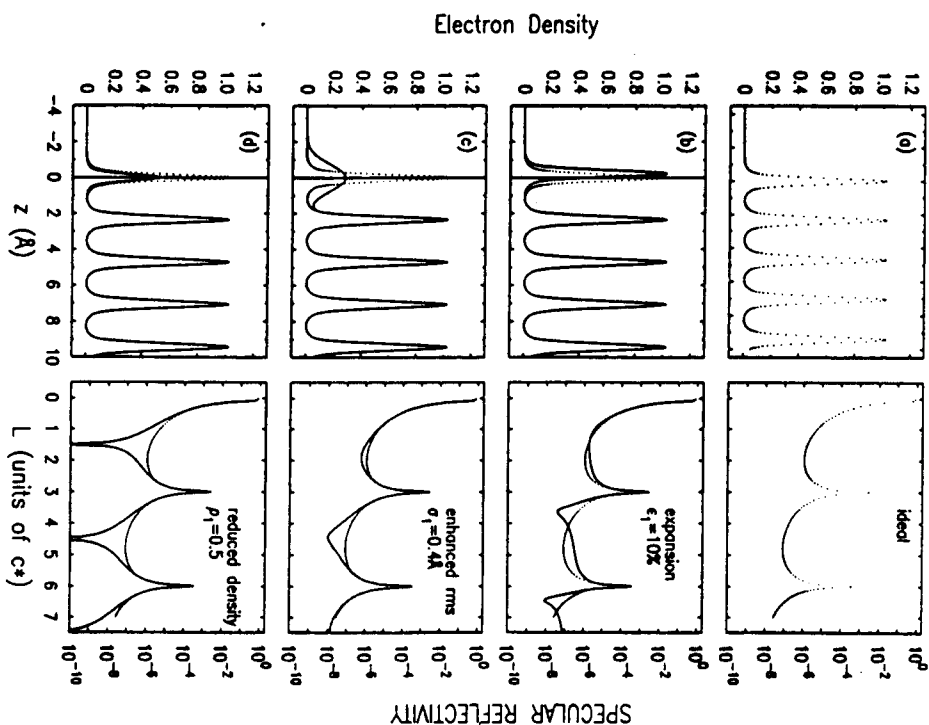


Figure 10. Real space density profiles (left) and calculated reflectivity spectra (right) for the  $Au(111)$  surface. (a) ideally terminated, (b - d) top layer modified, (b) expanded by 10%, (c) enhanced r.m.s. displacement amplitude, (d) 50% density. The ideally terminated profiles are shown as dotted curves.

phase. In Fig. 10d we show the density and reflectivity profiles for this model as solid lines and the ideal profiles are shown as dotted lines. The decreased top layer density model reflectivity curve (solid line) is always less than the ideal curve (dotted) and the reflectivity appears to go to zero at positions between Bragg peaks. Within the context of Eq. 4, at these half-order positions the magnitudes of the scattering amplitude from the top layer and from the sum of all the underlying layers are both  $\frac{1}{2}$  and these two amplitudes are exactly out of phase. Thus, this complete cancellation gives rise to zero reflectivity at these positions.

In the proceeding discussion, we have separately considered the effects of a top layer expansion, of an enhanced top layer r.m.s. displacement amplitude, and of a reduced top layer density. These three effects occur simultaneously at real interfaces and there is the added complication that not all of the underlying layers are ideally terminated gold layers. By carrying out least-squares fitting analysis of the profiles using a model which incorporates several surface layers which are not bulk like, many of these deviations can be extracted. Finally, we point out that at the electrochemical interface other species may form an adsorbed layer at the electrode surface whose scattering amplitudes interfere with the amplitude from the underlying gold layers. These species may include a metal monolayer (e.g., Pb), an anion layer (e.g.,  $I^-$ ), or possibly even a layer of water.

### 3.2.2. EXPERIMENTAL

In a reflectivity experiment, the scattered intensity is measured along the direction normal to the surface. These measurements are complicated by the fact that the the reflected intensity must be measured over a large dynamic range (e.g.,  $Q_z$ ) and this requires greater experimental care than in an ordinary diffraction measurement. For instance, the incident x-ray beam must not "spill-over" the edges of the crystal, the imperfect sample mosaic must be accounted for, and the diffuse scattering must be properly subtracted [11,17,26]. In order to avoid "spill-over" and to maximize the incident flux, the defining slits (before the sample) are adjusted to illuminate a region of less than 5 mm in length. The x-ray intensity on the sample is monitored by measuring the scattered intensity after the slits.

The resolution, in reciprocal space, is determined by the size of the incident beam, the size of the collected beam, and the sample mosaic [26,19,13,14]. In the present measurement, the detector acceptance of the scattered x-rays is controlled by a slit (2 mm by 10 mm) located 750 mm from the sample on the spectrometer  $2\theta$  arm. Since the incident beam was always less than 1 mm by 1 mm, the detector slit is the dominant factor determining the resolution.

The resolution volume is a three dimensional ellipsoid with three characteristic widths [10,11,27,17,26]. Two of these widths  $\Delta Q_2$  and  $\Delta Q_3$  are in the scattering plane of the spectrometer, defined by the rotation axis  $2\theta$ , and the third width  $\Delta Q_1$  is normal to the scattering plane. Within the scattering plane the resolution is determined mainly by the angular acceptance of the detector slit. The  $\Delta 2\theta$  full-width-half-maximum (FWHM) is given by the ratio of the slit size ( $\approx 2$  mm) to the distance between the slit and the sample ( $\approx 750$  mm). Typically,  $\Delta 2\theta$  (FWHM)  $\approx 2/750$  rads which is about  $0.15^\circ$ . The resolution function defined by these slits has a "box-like" profile where the width,  $\Delta Q_3$  (HWHM), equals  $\frac{1}{2} \cos(\theta) \Delta \theta$  (HWHM) and where  $\Delta \theta$  (HWHM)  $= \frac{1}{4} \Delta(2\theta)$  (FWHM).

At  $\lambda = 1.24 \text{ \AA}$  (10 keV),  $\Delta Q_2 \approx 0.007 \text{ \AA}^{-1}$ . By construction, the in-plane transverse resolution,  $\Delta Q_2$  (HWHM)  $\approx \Delta Q_3 \sin \theta$  (HWHM). Thus,  $\Delta Q_2$  is always smaller than  $\Delta Q_3$ . Normal to the scattering plane, the resolution was typically determined by 10 mm wide detector slits located on the detector arm. This yields a width,  $\Delta Q_1$ , which is about  $0.08 \text{ \AA}^{-1}$  (HWHM). We note that the diffuse background intensity which often obscures the reflectivity is proportional to the detector slit area. In order to reduce the background scattered intensity, this 10 mm wide slit width is often reduced to 5 mm.

Typical  $\theta$  rocking curves, along the specular direction at fixed  $2\theta$  values, are shown in Fig. 11. The curves were taken in  $0.01 \text{ M K I}$  at  $-0.15 \text{ V}$ . The values of  $L$  given in the figure correspond to the values at the center of the rocking curves. These diffraction profiles exhibit a sharp peak when the specular condition,  $\theta = \frac{1}{2}(2\theta)$ , is satisfied. Note that the rocking curves are broadest at small  $L$ . At large  $L$  the widths are close to the spectrometer resolution.

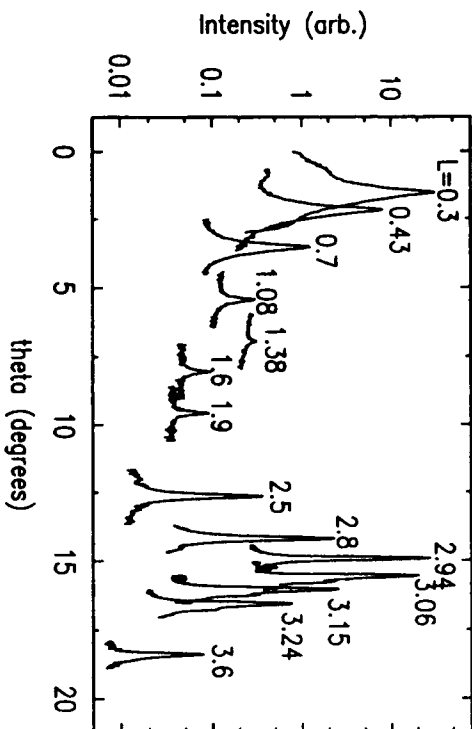


Figure 11. Typical rocking curves, along the specular direction, in  $0.01 \text{ M KI}$  at  $-0.15 \text{ V}$ .

We have fitted the rocking curves, shown in Fig. 11, to a Lorentzian profile with a width  $\delta\theta$ , convoluted with the resolution function, in order to extract the intrinsic peak width. In Fig. 12a, the fitted width is shown versus  $L$ . At small  $L$ ,  $\delta\theta = 0.15^\circ$  and decreases

to less than  $0.01^\circ$  at the largest values of  $L$ . The effect of the resolution function is minimal at small  $L$ , and becomes very significant at large  $L$ . Close to the Bragg peaks the underlying layers contribute significantly to the diffracted intensity and the rocking curves are narrowest.

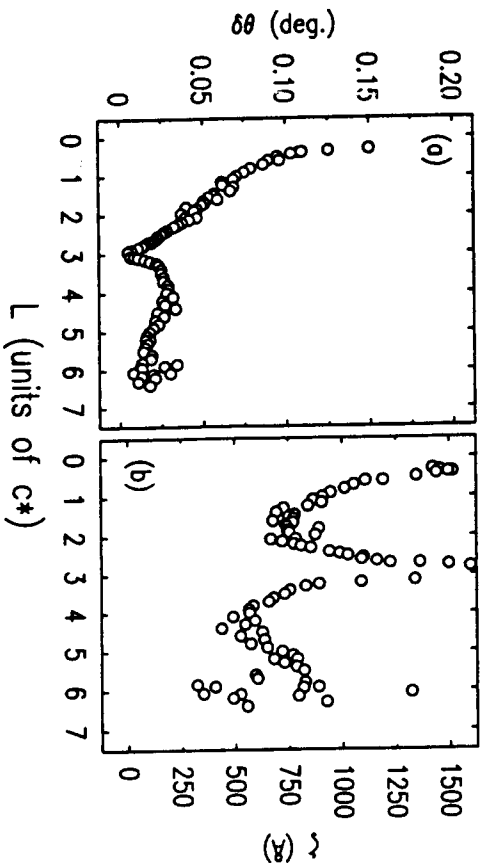


Figure 12. (a) Lorentzian rocking curve width,  $\delta\theta$ , and (b) coherence length  $\zeta$  versus  $L$  for 0.01 M KI at -0.15 V.

In a diffraction measurement, the coherence length  $\zeta$  is equal to the inverse diffraction width (e.g.,  $\Delta q^{-1}$ ). The coherence length,  $\zeta = (Lc^*\delta\theta)^{-1}$ , calculated from  $\delta\theta$  (see Fig. 12a), is shown in Fig. 12b. Far from the Bragg peaks, the coherence length corresponds to the effective surface length over which reflected x-rays are coherent. The calculated coherence length varies with  $L$  and ranges from about 500 to 1500 Å. Midway between the Bragg peaks the contribution to the reflectivity from the underlying layers is diminished and this leads us to conclude that the surface coherence length is around 500 Å. This length is slightly larger than the width calculated from in-plane diffraction measurements.

To account for the spatial variations of the sample mosaic and the effect of the coherence length on the widths of the rocking curve, it is necessary to integrate the scattered intensity over a range of  $\theta$  at constant  $2\theta$  as described above. The scan range must be broad enough

to calculate the integrated intensity after background subtraction. Typical  $\theta$  scans are shown in Fig. 11. Since the out-of-plane resolution,  $\Delta Q_z \approx 0.08$  Å (HWHM), is at least an order of magnitude broader than the transverse width from the Au surface,  $(Lc^*\delta\theta)$ , calculated from the rocking curves, the spectrometer automatically integrates over the out-of-plane direction. Under these conditions, we have previously shown [26] that the absolute reflectivity is given by

$$R(L) = \frac{\int d\theta I_s(\theta)}{\int d(2\theta) I_0(2\theta)} \quad (5)$$

where  $I_s(\theta)$  is the scattered intensity after background subtraction and  $I_0(2\theta)$  is the direct beam intensity. It is often difficult to measure  $I_0(2\theta)$  accurately since the full incident beam saturates the detector. For practical purposes, we choose the reflectivity normalization by insisting that the reflectivity agrees with the idealized reflectivity profile close to Bragg peaks. At these positions the reflectivity is almost completely insensitive to the details of the surface normal structure since many gold layers are contributing in the sum over the atomic layers. Previously, it has been shown that both normalization techniques yield identical results [19]. In order to integrate the rocking curves, the curves were fitted to a Lorentzian lineshape with a sloping, adjustable background.

### 3.2.3. RESULTS OF REFLECTIVITY STUDIES

Before presenting the experimental reflectivity profiles, the potential dependence is presented at fixed  $L$ . These results demonstrate that anion effects must be incorporated into the specular reflectivity models [13]. In Fig. 13, the potential dependence of the specular reflectivity is shown at (0, 0, 2, 2). These curves were obtained in 0.01 M solution of NaF, NaCl, and KBr, at a slew rate of 1 mV/sec. Scans at (0, 0, 3/2), exactly half-way between the (0, 0, 0) and (0, 0, 3) Bragg peaks, exhibit very similar potential dependence as at (0, 0, 2, 2). At the most negative potentials the surface is reconstructed and the absolute reflectivity equals  $1.56 \pm 0.05 \times 10^{-6}$  in all three solutions. The decrease in the reflectivity at (0, 0, 2, 2), in the positive sweep, results from the transition from the reconstructed phase to the (1 × 1) phase and from the adsorption of anions at the gold interface. This intensity decrease is larger in the KBr electrolyte than in the NaCl electrolyte, since bromine atoms have more electrons contributing to the scattering amplitude than chlorine atoms. In NaCl solution, the capacitance peak extends beyond 0.3 V which implies that the adsorbed chloride layer is not saturated up to 0.3 V. Correspondingly, the reflectivity at (0, 0, 2, 2) continues to decrease as the potential is extended beyond 0.3 V as more chloride is adsorbed. Because the adsorption-desorption of anions at the gold surface is reversible and occurs rapidly upon changing the potential, the reflectivity versus potential curves obtained from both sweep directions overlap at the potentials above 0.3 V. In order to account for the effects of solution species at the gold interface and potential induced changes in the structure of the gold layers the reflectivity model given by Eq. 4 must be extended.

To accommodate the adsorbed solution layer [13], the specular reflectivity is expressed as

$$RL = Q_i/c^2 = |r(Q_i)|^4 \left| \frac{256\pi^2 r_z^2}{3a^2 Q_z^2} \right| e^{Q_{\text{ad}}/Q_i} |S(L)|^2 \quad (6)$$

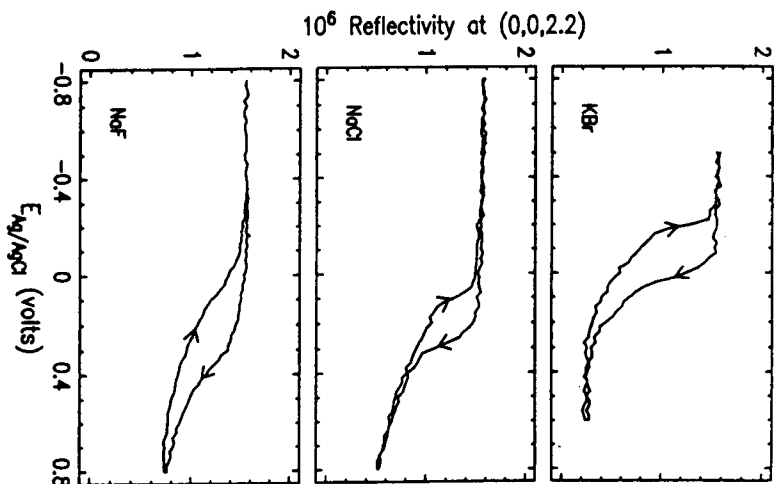


Figure 13. Potential dependence of the reflectivity at (0,0,2,2) on an absolute scale in 0.01 M solutions of  $KBr$ ,  $NaCl$ , and  $NaF$  in the positive and negative sweep directions. The potential independent reflectivity at low potentials corresponds to the reconstructed phase. The decrease in reflectivity in the positive going sweep corresponds to the transition to the  $(1 \times 1)$  state and anion adsorption.

$$S(L) = Z_0 \rho_0 e^{-iQ_z^2 \sigma_0^2 iQ_z d_0} + F_{Au}(Q_z) \left( \rho_1 e^{-iQ_z^2 \sigma_1^2 iQ_z d_1} + \sum_{n=1}^{\infty} e^{-iQ_z^2 \sigma_B^2 iQ_z n d} \right) \quad (7)$$

The first term in Eq. 7 corresponds to the scattering amplitude from a surface ion/water monolayer with a molecular charge  $Z_0$  (fixed in the analysis), an atomic layer density  $\rho_0$

relative to a  $Au(111)$  atomic layer, and a root-mean-square (r.m.s.) atomic displacement amplitude,  $\sigma_0$ . Here the magnitude of the scattering amplitude from each gold layer equals the gold form factor,  $F_{Au}$ , which equals 74 at small  $Q_z$ . The deviation from 79 is because not all of the electrons are considered free electrons at 8 keV [10]. Correspondingly, the magnitude of the scattering amplitude for an adsorbed monolayer ( $\rho_0 = 1$ ) is  $Z_0$  which equals 10, 17, 35, and 53 for water, fluorine, chlorine, bromine, and iodine, respectively.

The absorption losses from the polypropylene window and the thin electrolyte layer have been accounted for by assuming a slab of adsorbing material of constant thickness. This produces the factor  $e^{-Q_{zz}/Q_z}$ , where  $Q_{zz}$  is related to the thickness, density, and mass absorption cross sections of these layers. In the subsequent analysis, the absorption correction given in Eq. 6,  $Q_{zz}$ , is fixed at a value of  $0.2e^2$  for the  $NaF$ ,  $NaCl$ , and  $KI$  data and at a value of  $0.4e^2$  for the  $KBr$  data. Reflectivity within  $0.05e^2$  of the Bragg peaks and below  $0.4e^2$  has been excluded from the fitting procedure. In the first case, the kinematic approximation does not apply near Bragg peaks and in the latter case it is difficult to control the footprint of the incident beam on the sample at small angles.

In order to understand the effects of adsorbed species at the  $Au(111)$  surface, it is useful to directly compare the electrochemical results with the calculated profiles from an ideally terminated surface and from the vacuum  $(23 \times \sqrt{3})$  surface [19]. In Fig. 14a, the ideally terminated curve (dotted) does not exhibit the asymmetry around the Bragg peak and cannot describe all of the features of the data. The asymmetry around the Bragg peaks is most apparent in Fig. 14c in which the reflectivities have been normalized to the ideally terminated reflectivity profile. Since both the vacuum and electrochemical data support the same  $(23 \times \sqrt{3})$  motif, we believe that the scattering from the gold layers should be the same for both interfaces. The reconstructed vacuum model ( $\sigma_1 = 0.15 \text{ \AA}$ ,  $\rho_1 = 1.045$  and  $\epsilon_1 = -d_1/d = 3.3\%$ ) shown in Fig. 14a and 14c as a dashed line, exhibits the same asymmetry around the Bragg peaks. However, the model fails to describe the data between  $L = 0.5$  and  $2.5$ . This discrepancy is most apparent when the reflectivity is normalized to the reflectivity for the ideally terminated interface (Fig. 14c). An improved description of the specular reflectivity, in the reconstructed potential range for all three electrolytes, is obtained if we incorporate a single water layer. In the analysis we have fixed the molecular charge,  $Z_0 = 10$  (water). The parameters for the top gold layer were set to values obtained in vacuum ( $\rho_1 = 1.045$ , and  $\epsilon_1 = 3.3\%$ ); and we have allowed  $\rho_0$ ,  $d_0$ , and  $\sigma_0$  to vary. All three data sets are very well described by a model with  $\rho_0 = 1.0 \pm 0.2$ ,  $\sigma_0 = 0.60 \pm 0.15 \text{ \AA}$  [30], and a gold-water layer separation of  $2.9 \pm 0.3 \text{ \AA}$  given by the solid lines in Fig. 14a and 14c. A density of  $\rho_0 = 1.0$  for water only represents 13% of the electron density for the underlying gold layers. This water density is larger than the expected layer density ( $0.75$ ) calculated from the water volume ( $30 \text{ \AA}^3$  per water molecule) raised to the  $2/3$  power. We note that it is difficult to distinguish between a water layer and submonolayers of adsorbed ions since both contribute to the electron densities.

The present model of the specular reflectivity (Eq. 7), including the effects of a water monolayer, also describes the reflectivity from the  $Au(111)$  surface in the  $(1 \times 1)$  phase at positive potentials in  $NaF$ . Within the context of this model, the best fit is represented by a gold-water layer spacing of  $2.9 \text{ \AA}$  an r.m.s displacement amplitude of the water layer,  $\sigma_0 = 0.64 \text{ \AA}$  [30] and a water layer density of  $1.0 \pm 0.2$ . There is no apparent relaxation

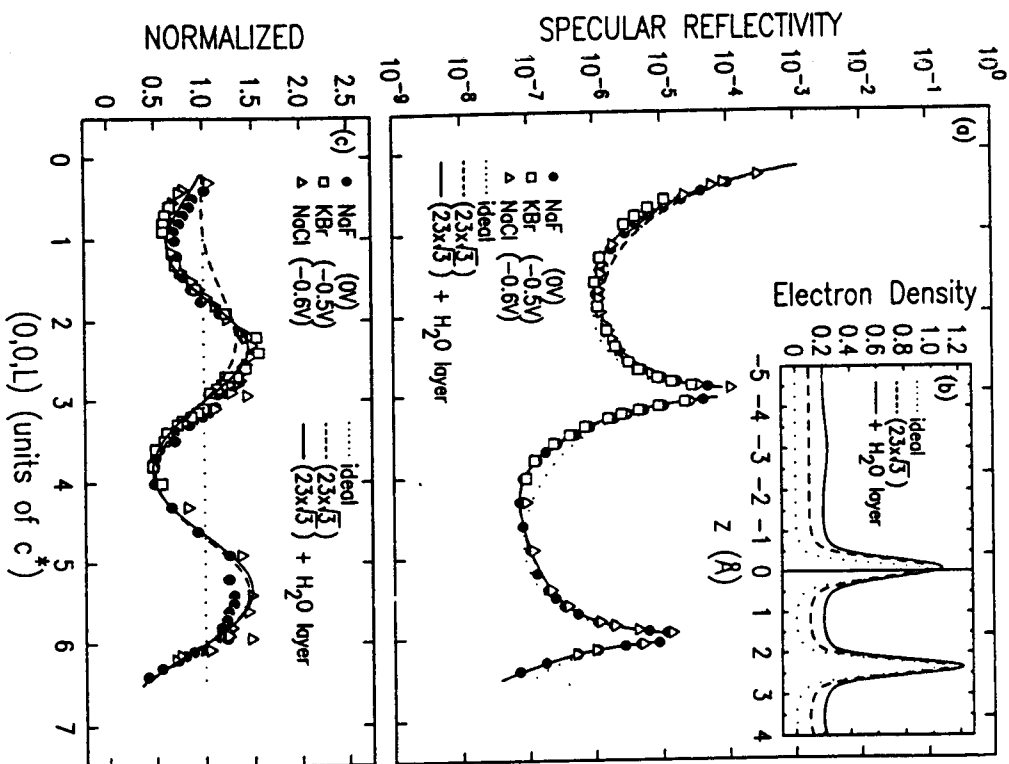


Figure 14. (a) Absolute specular x-ray reflectivity from the Au(111) surface in 0.01 M solutions of KBr, NaCl and NaF in the reconstructed phase. Calculated reflectivity profiles are shown for the ideally terminated surface (dotted line), the  $(23 \times \sqrt{3})$  reconstructed surface (dashed line) and for the  $(23 \times \sqrt{3})$  reconstructed surface with a water layer (solid line). (b) Corresponding real space density models. The density bump at about 3 Å corresponds to the water layer. For graphical purposes, some of the curves have been shifted upward. (c) X-ray reflectivity normalized to the reflectivity from the ideally terminated surface.

of the top gold-gold interlayer spacing and the r.m.s displacement amplitude of the top gold layer,  $\sigma_1$ , is 0.12 Å in the  $(1 \times 1)$  potential regime. Extending the model to include a second water layer does not improve the quality of the fit and suggests that the first layer density is close to unity. This density is somewhat higher than the expected density of 0.75.

The introduction of a boundary condition, such as a metal wall, modifies the bulk liquid structure in the vicinity of an interface [31-34]. In addition to this steric effect, the surface electric fields may reorient the dipole moments at the interface. Far from criticality, it has been predicted that the ordering induced by the wall should decay away with a characteristic length scale of the molecular size [35]. The structure of water near an electrode surface has been studied using analytic theory, and Monte Carlo and Molecular Dynamics simulation. For an updated bibliography of these studies see Ref. 34. The present results strongly suggest that ordered water near the gold interface modifies the x-ray reflectivity profiles. Detailed analysis provides information on the water layer density, the water-metal layer spacing and the width of the water layer (e.g. the r.m.s displacement amplitude). These results appear to be consistent with some of simulation results. At present, we can not detect the small change in the water-metal layer spacing which should occur with potential that are associated with the reorientation of the water dipoles. Also, the present data does not allow us to speculate on the nature of the water layers beyond the first layer. Studies which utilize electrodes with smaller  $z$  will lead to a larger change in the reflectivity in the presence of ordered water layers. Preliminary studies by Toney and coworkers indicate that the top layer of water may have a density which is twice that of ordinary water at the Ag(111) surface [36]. This large water density is not supported by our data.

The specular reflectivity profiles in the  $(1 \times 1)$  potential region in KBr (0.5 V) and NaCl (0.6 V) have been fitted with the same single layer model. Here,  $Z_0$  is fixed at 35 and 17 for the bromide and chloride anions, respectively. In the analysis, we allowed the three additional parameters describing the adsorbed anion layer ( $\rho_0$ ,  $d_0$ , and  $\sigma_0$ ) and the parameters describing the top gold layer ( $\sigma_1$  and  $d_1$ ) to vary in the least-squares-fitting procedure. All of the remaining parameters have been constrained at their bulk values. The fitted model is described by an anion layer with r.m.s displacement amplitudes ( $\sigma_0$ ) 0.47 Å (bromide) and 0.49 Å (chloride) [30]. The fitted atomic layer densities ( $\rho_0$ ) are 0.50 (bromide) and 0.67 (chloride). In both electrolytes the r.m.s displacement amplitudes of the top gold layer,  $\sigma_1 = 0.15$  Å is slightly smaller than the reconstructed value. The gold-bromide and gold-chloride layer spacings are  $2.4 \pm 0.3$  Å. This spacing is larger than the gold-gold layer spacing. Finally, we note that there is no apparent relaxation of the gold-gold layer spacing for the top gold layer (within 0.5%).

For iodine adlayers, the coverage obtained from the specular reflectivity analysis can be directly compared with the coverage calculated from the in-plane diffraction [25]. This comparison provides a stringent test of the reflectivity analysis. In Fig. 15 we show the specular reflectivity in 0.01 M KI at -0.15 V (closed circles) in the  $(p \times \sqrt{3})$  phase. As previously demonstrated, this deviation results from the destructive interference of specifically adsorbed anion layers. For iodine adlayers,  $Z_0 = 53$ , this effect is more significant than with Cl or Br adlayers. The best fit at -0.15 V gives  $\rho_0 = 0.38$  which was very

close to the value of  $\theta$  obtained from the in-plane diffraction ( $\theta = 0.37$  at  $-0.15$  V). In the subsequent analysis,  $\rho_0$  was set at 0.37 and we allowed  $\sigma_0$ ,  $\sigma_1$ ,  $d_0$ , and  $d_1$  to vary in the analysis. The best fit was obtained with  $\sigma_0 = 0.26$  Å,  $\sigma_1 = 0.14$  Å, with a top most interlayer gold spacing which is 1% greater than the bulk spacing and with a Au-I interlayer spacing equal to 2.3 Å. The Au-I interlayer spacing can be estimated in terms of the covalent bonding radii of gold (1.44 Å) and iodine (1.33 Å). If we assume that all of the iodine atoms are in "A top," "bridge," or "hollow" sites, then the interlayer spacings are 2.77, 2.36, 2.21 Å, respectively. However, in the  $(p \times \sqrt{3})$  phase the iodine atoms are at intermediate positions between "bridge" and "hollow" sites and we estimate an interlayer spacing of 2.28 Å which is the average of these two. This estimated Au-I interlayer spacing is very close to the measured value of 2.3 Å determined from the reflectivity analysis. Furthermore, this distance supports the assumption of covalent bonding between the Au and I.

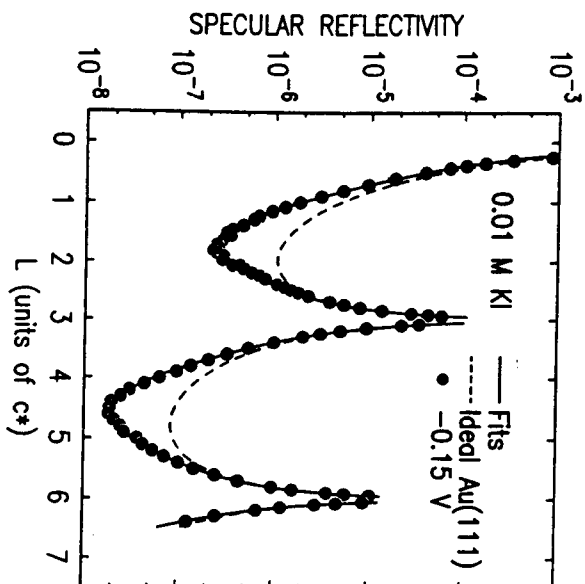


Figure 15. Absolute specular x-ray reflectivity from the Au(111) surface in 0.01 M KI at  $-0.15$  V in the  $(p \times \sqrt{3})$  adlayer phase.

In summary, specular reflectivity in the reconstructed phase suggests that there is a well-defined monolayer of water at the interface. In the  $(1 \times 1)$  phase, the adsorption of

anions has a drastic effect on the reflectivity and detailed analysis provides information on the coverage and position of this anion layer. Non specular reflectivity studies have confirmed that the phase transition from the  $(23 \times \sqrt{3})$  phase at low potential is to an ideally terminated  $(1 \times 1)$  phase at higher potential [13].

These studies demonstrate that specular reflectivity can provide detailed information about the surface normal structure at the Au(111) electrode. We note that the gold surface normal structures under electrochemical control [3,13,37] and ultra high vacuum conditions [19,26] are in good agreement for both the (111) and (001) surfaces. An important aspect of the x-ray reflectivity technique in electrochemistry is the sensitivity to adsorbed solution species and to the underlying electrode layers. This structural information can not be directly obtained from other techniques. Therefore, x-ray reflectivity is likely to play an important role in the quest to determine the structure of electrode surfaces.

#### 4. Acknowledgement

This work is supported by the Division of Materials Sciences, U.S. Department of Energy, under Contract No. DE-AC02-76CH00016. The Au(111) reconstruction study was carried out in collaboration with Hugh Isaacs and Alison Davenport (BNL/DAS). The bismuth study was carried out in collaboration with Chun-Chen, Keith Kepler, and Andy Gewirth (Univ. of Ill.). The iodine study was carried out in collaboration with Gavin Watson (BNL/Physics).

#### 5. References

1. M. G. Samant, M. F. Toney, G. L. Borges, L. Blum, and O. R. Melroy, *J. Phys. Chem.* **92**, 220 (1988); O. R. Melroy, M. F. Toney, G. L. Borges, M. G. Samant, J. B. Kortright, P. N. Ross, and L. Blum, *Phys. Rev. B* **38** 10962 (1988).
2. M. F. Toney, J. G. Gordon, M. G. Samant, G. L. Borges, D. G. Wiesler, D. Yee, and L. B. Sorensen, *Langmuir* **7** 796 (1991).
3. B. M. Ocko, J. Wang, A. Davenport, and H. Isaacs, *Phys. Rev. Lett.* **65**, 1466 (1990); B. M. Ocko and J. Wang, in *Proc. of the Workshop on Structural Effects in Electroanalysis and Oxygen Electrochemistry*, edited by D. Scherson, D. Tryk, M. Daroux, and X. Xing, *Electrochem. Soc., Pennington*, 1992, p. 147.
4. O. M. Magnussen, J. Hostlos, R. J. Nicols, R. J. Behm, and D. M. Kolb, *Phys. Rev. Lett.* **64**, 2929 (1990); T. Hachiyu, H. Honbo, and K. Itaya, *J. Electroanal. Chem.* **315**, 275, (1991); M. P. Green and K. J. Hanson, *Surf. Sci.*, **259**, L743 (1991); S.-L. Yau, X. Gao, S.-C. Chang, B. C. Schardt, and M. Weaver, *J. Am. Chem. Soc.*, **113**, 6049 (1991).
5. X. Gao, A. Hamelin, and M. J. Weaver, *J. Chem. Phys.*, **95**, 6993 (1991).
6. N. J. Tao and S. M. Lindsay, *J. Phys. Chem.*, **96**, 5213 (1992).
7. X. Gao, and M. J. Weaver, *J. Am. Chem. Soc.*, **114**, 8544 (1992).
8. S. Manne, P. K. Hansma, J. Massie, V. B. Elings, A. A. Gewirth, *Science*, **25**, 183 (1991).

9. C. H. Chen, S. M. Veecky, and A. A. Gewirth, *J. Am. Chem. Soc.*, **114**, 451 (1992).
10. B. E. Warren, X-Ray Diffraction, Addison-Wesley (1969).
11. R. Feidenhans'l, *Surf. Sci. Reports* **10**, 105 (1989); I. K. Robinson and D. J. Twest, *Rep. Prog. Phys.* **55**, 599 (1992).
12. M. F. Toney and O. R. Melroy, in *Electrochemical Interfaces: Modern Techniques for In-Situ Interface Characterization*, edited by H. D. Abruna, VCH Verlag Chemical, Berlin, 1991, p. 57; M. F. Toney, J. G. Gordon, and O. R. Melroy, *SPIE Proc.* **1550**, 147 (1991).
13. J. Wang, B. M. Ocko, A. J. Davenport, and H. S. Isaacs, *Phys. Rev. B*, **46**, 10321 (1992).
14. J. Wang, B. M. Ocko, A. J. Davenport, and H. S. J. Wang, A. J. Davenport, H. S. Isaacs, and B. M. Ocko, *Science*, **255**, 1416 (1992); J. Wang, B. M. Ocko, A. J. Davenport, H. S. Isaacs, in *X-Ray Methods in Corrosion and Interfacial Electrochemistry*, edited by A. J. Davenport and J. G. Gordon, *Electrochem. Soc., Pennington*, 1992, p. 34; B. M. Ocko, A. Gibaud, J. Wang, *J. Vac. Sci. Technol. A*, **10**, 3019 (1992).
15. J. L. Whitton and J. A. Davies, *J. Electrochem. Soc.*, **111**, 1347 (1964).
16. W. R. Busing and H. A. Levy, *Acta Cryst.*, **22**, 454 (1967).
17. I. K. Robinson, *Phys. Rev. B*, **33**, 3830 (1986).
18. S. G. J. Mochrie, *J. Appl. Cryst.*, **21**, 1-3 (1988).
19. A. R. Sandy, S. G. J. Mochrie, D. M. Zehner, K. G. Huang, and D. Gibbs, *Phys. Rev. B*, **43**, 4667 (1991); K. G. Huang, D. Gibbs, D. M. Zehner, A. R. Sandy, and S. G. J. Mochrie, *Phys. Rev. Lett.*, **65**, 3317 (1990).
20. A. Hamelin, *J. Electroanal. Chem.*, **142**, 229 (1992); J. P. Bellier and A. Hamelin, *C.R. Acad. Sci. (Paris)* **280**, 1489 (1975).
21. M. S. Zei, G. Lehmptuhl, and D. M. Kolb, *Surf. Sci.*, **221**, 23 (1989).
22. C. L. Fu and K. M. Ho, *Phys. Rev. Lett.*, **63**, 1617 (1989).
23. C. H. Chen, K. D. Kepler, A. A. Gewirth, B. M. Ocko, and J. Wang, *J. Phys. Chem.*, **97**, 7290 (1993).
24. B. G. Bravo, S. L. Michelhaugh, M. P. Soriaga, I. Villegas, D. W. Suggs, and J. L. Stickney, *J. Phys. Chem.*, **95**, 5245 (1991); R. L. McCarty and A. J. Bard, *J. Phys. Chem.*, **95**, 9618 (1991).
25. J. Wang, G. M. Watson, and B. M. Ocko, (accepted at *Physica B*).
26. D. Gibbs, B. M. Ocko, D. M. Zehner, and S. G. J. Mochrie, *Phys. Rev. B*, **38**, 7503 (1988); D. Gibbs, B. M. Ocko, D. M. Zehner, and S. G. J. Mochrie, *Phys. Rev. B*, **42**, 7330 (1990); B. M. Ocko, D. Gibbs, K. G. Huang, D. M. Zehner, and S. G. J. Mochrie, *Phys. Rev. B*, **44**, 6429 (1991).
27. A. Braslau, P. S. Pershan, G. Swislow, B. M. Ocko, and J. Als-Nielsen, *Phys. Rev. A*, **38**, 2457 (1988).

28. B. M. Ocko, *Phys. Rev. Lett.*, **64**, 2160 (1990).
29. S. P. Witherow, T. H. Barret, and R. J. Culbertson, *Surf. Sci.*, **161**, 584 (1985).
30. The r.m.s displacement amplitudes given are larger by a factor  $\approx \sqrt{3}$  than those given in ref. [13]. The present values have been modified because of a programming error which does not modify the fitted profiles..
31. P. A. Thiel and T. E. Madey, *Surf. Sci. Rep.* **7**, 211 (1987).
32. *Microscopic Models of Electrode-Electrolyte Interfaces*, edited by J. W. Halley and L. Blum, *Electrochem. Soc., Pennington*, 1993.
33. *Condensed Matter Aspects of Electrochemistry*, edited by M. P. Tosi and A. A. Koryshev, World Scientific, 1991.
34. J. D. Porter and A. S. Zinn, *J. Phys. Chem.* **97**, 1190 (1993).
35. B. J. Widom, *J. Stat. Phys.* **19**, 563 (1978).
36. Michael Toney, private communications..
37. I. M. Tidswell, N. M. Markovic, C. A. Lucas, and P. N. Ross, *Phys. Rev. B*, **47**, 16542 (1993).